Estimating magnetar radii with an empirical meta-model

Debarati Chatterjee* and Francesca Gulminelli LPC, UMR6534, ENSICAEN, F-14050 Caen, France

Debora P. Menezes UFSC, Dept de Fisica-CFM, Florianopolis, Brazil

December 17, 2018

Abstract

The presence of strong magnetic fields in neutron stars, such as in magnetars, may significantly affect their crust-core transition properties and the crust size. This knowledge is crucial in the correct interpretation of astrophysical phenomena involving magnetars, such as glitches in observed rotation frequencies, cooling, bursts and possibly tidal polarizabilities. A recently developed metamodelling technique allows exploring the model dependence of density functional theory equation of state calculations. In this work, we extend this metamodel to investigate the effect of strong magnetic fields on spinodal instabilities of neutron star matter and the associated crust-core properties. Both Tolman-Oppenheimer-Volkov and a full self-consistent numerical calculations are performed for the neutron star structure, the results being quantitatively different for strong magnetic fields.

1 Introduction

With the rapid advance of astrophysical techniques on compact objects observation, there is an increased need to improve theoretical modelling to accurately describe the associated observed phenomena. Following the recent launch of the NICER (Neutron Star Interior Composition Explorer) mission [1, 2], one expects to be able to measure neutron star radii to 5% accuracy. One may also expect improved estimates of the moment of inertia of neutron stars from gravitational wave observations [3]. However, improvements in theoretical estimates of neutron star radii or moment of inertia are limited due to the uncertainties in the properties of nuclear matter at high densities [4]. One such property is the density at which nuclear matter in neutron stars goes through a phase transition, from solid inhomogeneous matter in the crust to the homogeneous liquid phase in the core. Although the liquid-gas phase transition is well understood from the studies of homogeneous nuclear matter [5], in the case of neutron star matter the problem is more complex.

The understanding of the properties of the crust-core interface is important for accurate interpretation of several other astrophysical phenomena involving neutron stars. Explanations for glitches in the otherwise periodic rotational periods of neutron stars requires a knowledge of their elastic properties and crustal moment of inertia [6]. Thermal properties of the crust-core interface govern their cooling behavior [7]. Viscosity of the crust-core transition region also plays a major role in the emission of gravitational waves due to non-axisymmetric instabilities [8]. In 2017, the first detection of a gravitational wave, GW170817, generated by the collision of two neutron stars was confirmed by the LIGO and Virgo collaborations [9] and also observed in different regions of the electromagnetic spectrum, what was then called a multi-messenger event [10]. To reproduce GW170817 tidal polarizability [11, 12], besides the use of an appropriate equation of state, the size of the crust itself plays a non negligible role in the calculation of the Love number, which is a necessary step to compute the tidal polarizabilities of the neutron stars belonging to a binary system [13].

 $^{^*} d chatter jee@lpccaen. in 2p3. fr\\$

In non-magnetized neutron stars, the outer crust is generally described by the BPS equation of state [14] and the inner crust can be described by the BBP equation of state [15] or by a pasta phase region. Different calculations and numerical techniques can be used to investigate the crust-core region, the most common involving binodal sections, thermodynamical and dynamical spinodals [16] and the pasta phase transition to homogeneous phase [17], all of them converging to comparable transition densities [18]. The crust-core transition being an equilibrium phenomenon, a quantitative estimation of the transition point in principle demands a complete pasta phase calculation. However, such modelling is complex and it relies on a proper determination of the surface tension, a matter of debate in the literature, at least for the last 40 years [19]. To circumvent the pasta calculation, another possibility is to study the transition region from the properties of the homogeneous matter and its phase transition by determining the appearance of the instability region well described by spinodals. In this case, many properties of the crust-core interface and of the crust itself can be obtained directly from the transition densities and related thermodynamical quantities. According to well established calculations [20, 21, 22, 23, 24], many of the crust properties, as its moment of inertia, mass and radius can be directly computed from the equation of state at the transition boundary. In particular, it was shown in ref. [25], that the approximate results for the crust extracted from the core calculation up to the transition density lead to very accurate results for both its thickness and mass.

However the different microscopic (relativistic and non-relativistic) calculations give different predictions for the crust-core transition point [16, 26, 27]. These differences may arise either due to the differences in the underlying form of the density functionals inherent to the model or due to limitations in our knowledge of the empirical nuclear parameters extracted from experiments [28, 29]. Hence, the crust thickness is generally model dependent, but very important if one wants to study different astrophysical phenomena involving isolated or binaries of neutron stars.

Magnetars are a special class of isolated neutron stars bearing surface magnetic fields three orders of magnitude larger than their non-magnetized counterparts and slow rotation. Although just about 30 of them have been clearly identified [30] so far, they display a large number of peculiar phenomena, such as antiglitches, bursts and oscillations that challenge our understanding of neutron stars. It is well known that in the presence of strong magnetic fields, the motion of charged particles are affected, which in turn, alters the equation of state (EoS) [31] and related properties both in the core and the crust. Consequently the crust-core boundary of magnetars presents different features as compared with the usual one of neutron stars. Moreover, recent studies [32] indicate that during the cooling process of a magnetar, the crust-core transition region plays an important role in determining its final configuration. Another interesting calculation [33] points to quite a large crust (2.4 Km) for a 1.4 M_{\odot} neutron star, with non-negligible consequences on the cooling mechanism and on the emission of gravitational waves.

The crust-core region of magnetars has recently been studied within the relativistic mean field model framework [34, 35, 36]. In these works, the effects of strong magnetic fields $(10^{15} - 10^{17} \text{ G})$ on the instability region have been investigated with the help of the Vlasov formalism used to determine the dynamical spinodals. Although the magnetic fields at the surface of magnetars are of the order of $10^{14} - 10^{15}$ G [30], stronger fields can be expected in their interior. Assuming that the crust can be as large as it was computed in [33], fields of the order of 10^{17} G would be justified at the transition boundary.

In the present work, we revisit the problem of the crust-core boundary and the crust size in magnetars by studying thermodynamical and dynamical spinodal sections within different models and formalisms from the ones used in [34, 35, 36]. We use a meta-modelling technique based on the density functional theory, which consists of a general framework developed to take into account a huge variety of models usually used to describe nuclear and stellar matter [37, 38, 39]. The parameters of this meta-model are directly related to the empirical parameters that can be constrained through nuclear physics experiments [37]. This allows us to determine the most influential parameters governing the crust-core transition in the presence of strong magnetic fields, and to assess the model dependence of the results.

The relation between the EoS, the transition point, and the crustal thickness is complicated by the fact that the Tolman Oppenheimer Volkov (TOV) formalism of hydrostatic equilibrium in general relativity is not correct in the presence of strong magnetic fields, since they break the spherical symmetry assumed in the calculations that lead to the TOV [40]. In the present work, we employ a recently developed consistent formalism for constructing numerical models of neutron stars, considering magnetic field effects on the microscopic EoS and solving the Einstein-Maxwell and equilibrium equations to obtain the global neutron star structure.

This paper is organized as follows: in section 2, we describe the theoretical formalism for the microscopic calculations. In section 2.1 we recapitulate the details of this MetaModel (MM) approach for the Equation of State (EoS), while the technique for the determination of the crust-core (CC) transition point is detailed in section 2.2. We study the effect of strong magnetic fields on the CC point in section 3, and we examine the sensitivity to the most influential empirical parameters in the same section. We show in particular (section 3.2) that the influence of the poorely constrained derivatives of the symmetry energy (L_{sym}, K_{sym}) dramatically increases with the increase of the magnetic field. The effect of magnetic fields on the neutron star structure is explored in Sec. 4, and we show that going beyond the spherical TOV approximation is very important not only for the determination of the M(R) relation [40, 41, 42], but also for the determination of the crustal properties even for relatively low magnetic fields. Finally we infer the conclusions of the study in section 5.

2 Theoretical formalism for the microscopic model

In this section, we elaborate on the theoretical approach employed to describe the microscopic neutron star matter. In section 2.1, we highlight the fundamental aspects of the MM, that was originally proposed in [37], and applied to study neutron stars [38, 28, 29] as well as nuclei [39]. In the following Sec. 2.2, we apply this MM to study the phase transition properties and to determine the crust-core phase boundary.

2.1 Meta-modelling approach for EoS

In previous works on the effect of the magnetic field on the crust-core phase transition [34, 35, 36], EoS functionals extracted from the relativistic mean-field approach were employed. To have a complementary view on the subject, in this work we take a wide range of reference models, some the most widely used and realistic non-relativistic functionals, namely the Skyrme functional SLy5 and SLy4 [43], Bsk17 [44] as well as the relativistic model TM1 [45]. The choice was inspired by the fact that their values of slope of symmetry energy cover a wide range, which is known to influence crust-core transition properties [16, 28].

In order to explore these different models, we will use the technique proposed in ref. [37], where a generic meta-modelling of the nuclear EoS was introduced. In that reference, a flexible fully analytical functional was proposed with a parameter space large enough to be able to accurately reproduce different EoS functional forms from phenomenological as well as ab-initio calculations. By changing the parameter set of the meta-functional, one is then able to switch between different models with a very limited computational effort. Moreover, since all the parameters can be independently varied, interpolations are possible between the different models and sensitivity studies can be done, in order to assess the relative influence of the parameters on a given observable. We will take advantage of this property of the meta-modelling in section 3.2.

The energy per particle of homogeneous nuclear matter at baryonic density $n = n_n + n_p$ and asymmetry $\delta = (n_n - n_p)/n$ is expressed as:

$$e_{HNM}(n,\delta) = e_{kin}^p + e_{kin}^n + \sum_{\alpha=0}^4 (a_{\alpha is} + a_{\alpha iv}\delta^2) \frac{1}{\alpha!} \left(\frac{n - n_{sat}}{n_{sat}}\right)^\alpha u_\alpha(n,b) . \tag{1}$$

In this expression, n_{sat} is the saturation density of symmetric matter, e_{kin_q} , q = n, p is the kinetic energy functional

$$e_{kin}^{q} = \frac{3\hbar^2}{10m_a^*} \left(\frac{3\pi^2 n}{2}\right)^{2/3} (1 + \tau_3 \delta)^{2/3} \tag{2}$$

and the in-medium neutron and proton effective masses m_n^* and m_p^* are also expanded in terms of the density parameter x as [37]:

$$\frac{m}{m_a^*} = 1 + (\kappa_{sat} + \tau_3 \kappa_{sym} \delta) \frac{n}{n_{sat}},\tag{3}$$

where $\tau_3 = 1$ for neutrons and -1 for protons. The $a_{\alpha,is}$ and $a_{\alpha,iv}$ parameters fulfill a one-to-one mapping with the so-called empirical parameters, given by the successive derivatives around saturation n_{sat} of the isoscalar $(E_{sat}, K_{sat}, Q_{sat}, Z_{sat})$ and isovector $(E_{sym}, L_{sym}, K_{sym}, Q_{sym}, Z_{sym})$ part of the energy functional. Finally, $u_{\alpha}(n,b)$ is a low-density correction that insures the correct zero density limit of the functional, and becomes negligible at a density $n_{min} \ll n_{sat}$. The value of n_{min} is governed by the extra parameter b of the model.

This meta-functional was fitted to a large number of relativistic and non-relativistic nuclear models, and the corresponding parameter sets $\{\vec{X}\}=\{n_{sat},\,E_{sat},\,E_{sat},\,E_{sat},\,E_{sat},\,E_{sym$

A fit of the b parameter on the spinodal curve was performed for a few reference models, including SLy5 and SLy4, in [29]. In addition to that, in that work, a posterior distribution of the b parameter was obtained within a complete Bayesian analysis, under the constraint that the different functionals described by the meta-modelling parameter space should all fall within the uncertainty interval obtained at low densities from the ab-initio effective field theory calculations of ref.[46]. The best reproduction of the original Skyrme models was found for $b = 10/3log2 = \sim 2.31$ so we will use this optimized value for the rest of this study.

When dealing with inhomogeneous matter as in Section 2.2 below, the meta-functional is extended by adding two extra gradient terms[39]:

$$e(n,\delta) = e_{HNM}(n,\delta) + \sum_{q=n,p} \frac{\hbar^2}{2m_q^*} \frac{\tau_{2q}}{n} + C_{fin} \frac{(\nabla n)^2}{n} + D_{fin} \frac{(\nabla(n\delta))^2}{n}.$$
 (4)

The $\tau_{2q} = \tau_{2q}^l + \tau_{2q}^{nl}$ are second order local and non-local corrections arising from an \hbar expansion

of the kinetic energy density of an inhomogeneous system:

$$\tau_{2q}^{l} = \frac{1}{36} \frac{(\nabla n_q)^2}{n_q} + \frac{1}{3} \Delta n_q \tag{5}$$

$$\tau_{2q}^{nl} = \frac{1}{6} \frac{\nabla n_q \nabla f_q}{f_q} + \frac{1}{6} n_0 \frac{\Delta f_q}{f_q} - \frac{1}{12} n_q \left(\frac{\nabla f_q}{f_q}\right)^2, \tag{6}$$

with $f_q = m/m_q^*$. The C_{fin} (D_{fin}) parameters govern the isoscalar (isovector) surface properties of the energy functional in the linear response approximation. Such terms appear explicitly in Skyrme functionals, and their values are determined in the fitting protocol of Skyrme parameters to nuclear ground state properties, together with the other parameters of the functional. In the case of the meta-modelling representation of non-Skyrme functionals, we determine the values of C_{fin} and D_{fin} through a χ^2 fit of the masses of a set of magic and semi-magic nuclei, where the theoretical masses are calculated in the Extended-Thomas-Fermi spherical approximation with the meta-functional using a parametrized density profile [29].

The resulting bulk and surface parameters are reported in table 1 and 2 for the functionals used in this work.

Table 1: Empirical parameters for reference models

Model	n_{sat}	E_{sat}	K_{sat}	Q_{sat}	Z_{sat}	E_{sym}	L_{sym}	K_{sym}	Q_{sym}	Z_{sym}	m^*/m	$\Delta m/m$
SLy5	0.1604	-15.98	230	-364	1592	32.03	48.3	-112	501	-3087	0.70	-0.18
SLy4	0.1595	-15.97	230	-363	1587	32.01	46.0	-120	521	-3197	0.69	-0.19
TM1	0.1450	-16.26	281	-285	2014	36.94	111.0	34.0	-67.	-1546.0	0.71	-0.09
Bsk17	0.1586	-16.05	242	-364	1460	30.00	36.3	-182	451	-2508	0.80	0.04

Table 2: Surface parameters for reference models

Model	$C_{fin}(MeVfm^5)$	$D_{fin}(MeVfm^5)$
SLy5	56.25	23.95
SLy4	122.68	185.31
TM1	55.0	100.
Bsk17	35.0	10.

2.2 Crust-core phase transition (CCPT) properties

Once the meta-functional for the baryonic energy of section 2.1 is specified, the crust-core phase transition can be inferred from the instability properties of the functional. A first rough definition of the transition point can be obtained from the spinodal instability which is associated to the liquid-gas phase transition in neutral nuclear matter at sub-saturation densities [47]. The spinodal region is defined as the convex part of the energy density in the neutron-proton density plane, and can be spotted from the presence of negative eigenvalues of the following curvature matrix:

$$C_{NM} = \begin{pmatrix} \partial \mu_n / \partial \rho_n & \partial \mu_n / \partial \rho_p \\ \partial \mu_p / \partial \rho_n & \partial \mu_p / \partial \rho_p \end{pmatrix}$$
 (7)

i.e., the curvature matrix depends on the energy functional via the chemical potentials $\mu_q = \partial \epsilon / \partial n_q$, (q = n, p).

The thermodynamic spinodal only gives a qualitative estimation of the transition point. Indeed, in the presence of an electron background gas, the liquid-gas phase transition of nuclear matter is replaced by a transition from an homogeneous medium to a clusterized one. Such a transition is better signalled by the instability of nuclear matter against independent fluctuations of neutron, proton and electron densities with a finite spatial extension[47, 48]. The energy density curvature matrix subject to finite size density fluctuations, takes the form

$$C_{f} = \begin{pmatrix} \partial \mu_{n} / \partial \rho_{n} & \partial \mu_{n} / \partial \rho_{p} & 0 \\ \partial \mu_{p} / \partial \rho_{n} & \partial \mu_{p} / \partial \rho_{p} & 0 \\ 0 & 0 & \partial \mu_{e} / \partial \rho_{e} \end{pmatrix} + k^{2} \begin{pmatrix} C_{fin} & D_{fin} & 0 \\ C_{fin} & C_{fin} & 0 \\ 0 & 0 & 0 \end{pmatrix} + \frac{4\pi e^{2}}{k^{2}} \begin{pmatrix} 0 & 0 & 0 \\ 0 & 1 & -1 \\ 0 & -1 & 1 \end{pmatrix}$$

In this matrix, in addition to the bulk term that corresponds to the thermodynamic spinodal, there is a surface term proportional to the square of the wavelength k, while the Coulomb interaction adds a term inversely proportional to k^2 . Then thermodynamic fluctuations are recovered at $k \to \infty$ limit of this model. The global instability region is defined as the envelope of the different k-spinodals corresponding to all the possible linear sizes for the density fluctuation.

For both thermodynamic eq.(7) and dynamic eq.(8) spinodals, the crust-core transition point is defined as the intersection of the instability envelope with the neutrino-less β -equilibrium curve of neutron star matter, defined by:

$$\mu_n - \mu_p = \mu_e. \tag{8}$$

2.3 Introduction of the magnetic field

It is well known that in the presence of strong magnetic fields, the motion of charged particles is confined to Landau levels, in a direction perpendicular to the magnetic field direction. This leads to a modification of the energy levels of the particles, and hence of the EoS of neutron star matter [31].

In the formulation of the meta-modelling eq.(1), a modification of the single-particle levels directly affects the first term of the meta-functional, which physically corresponds to the kinetic energy per baryon in the non-relativistic approximation. Within this approximation, the kinetic energy per baryon of neutrons remains unaltered, i.e.

$$e_{kin}^{n} = \frac{3\hbar^{2}}{10m_{n}^{*}} \left(\frac{3\pi^{2}n}{2}\right)^{2/3} (1+\delta)^{5/3}$$
(9)

where m_n^* from eq.(3) is the effective neutron mass. Conversely, electrons and protons are affected by the magnetic field. For the electrons, we follow the standard relativistic treatment of ref.[49]. Within

the non-relativistic approximation [50], the single particle energy of the ν -th Landau level is given by

$$\mu_p^* = \frac{p_{z,F}^2}{2m_p^*} + \frac{\nu eB}{m_p^*} \,, \tag{10}$$

where p_z is the momentum of the proton in the z-direction in which the magnetic field is directed. The proton density becomes modified in presence of the magnetic field as:

$$n_p = \frac{eB}{2\pi^2} \sum_{\nu}^{\nu_{max}} g_{\nu} p_{z,F}(\nu)$$
 (11)

where the maximum number of Landau levels is given by:

$$\nu_{max} = \frac{m_p^* \mu_p^*}{eB}.\tag{12}$$

Then the proton contribution to the kinetic energy per baryon becomes:

$$e_{kin}^{p} = \frac{eB}{2n\pi^{2}} \frac{1}{m_{p}^{*}} \sum_{\nu}^{\nu_{max}} \left[\frac{p_{z,F}^{3}(\nu)}{3} + 2\nu eBp_{z,F}(\nu) \right] . \tag{13}$$

When the magnetic field is high, only the lowest or a few Landau levels are occupied. The corresponding critical quantizing field B_c can be calculated by equating the rest energy mc^2 of a particle of mass m to its cyclotron energy $\hbar\omega_c$, where $\omega_c=eB/mc$ is the cyclotron frequency, i.e. $B_c=m^2c^3/e\hbar$. For the case of electrons, this gives $B_c^e=4.4\times 10^{13}$ G. For low magnetic fields, the Landau levels are numerous and closely spaced, such that one recovers the continuum limit in the absence of the field.

3 Results: Magnetic field effects

3.1 Effect on the CCPT

We first analyze the effect of the magnetic field on the thermodynamical spinodal for our reference model SLy5. The results of this section are in qualitative agreement with the previous works [34, 35, 36] using relativistic mean-field functionals, and the Vlasov method to compute the dynamical spinodal.

Taking multiples of the quantizing electron field $B_c^e = 4.4 \times 10^{13}$ G, we express the magnetic field in units of $B_* = B/B_c^e$. The effect of the magnetic field on the thermodynamical spinodal is shown in Fig. 1. It is found to be negligible up to $10^2 B_c^e$. However, for fields above $10^3 B_c^e$, the effect of magnetic field on the thermodynamical spinodal region is quite dramatic. Instead of a single region, we now find alternate regions of stability and instability. This is due to the appearance of kinks in the EoS as a result of the confinement of the motion of the charged particles to quantized Landau levels.

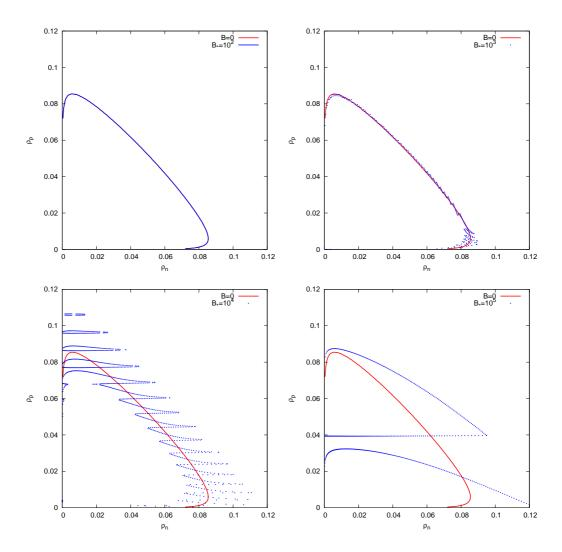


Figure 1: Thermodynamic spinodals for relative magnetic field strengths $B_* = 10^2$ (upper left), 10^3 (upper right), 10^4 (lower left) and 10^5 (lower right). The continuous red line gives the spinodal envelope in the absence of magnetic field.

We now turn to investigate how magnetic field affects the CCPT for the thermodynamical and dynamical spinodals. As already discussed in section 2.2, the CCPT is determined from the crossing of the spinodals with the β -equilibrium line.

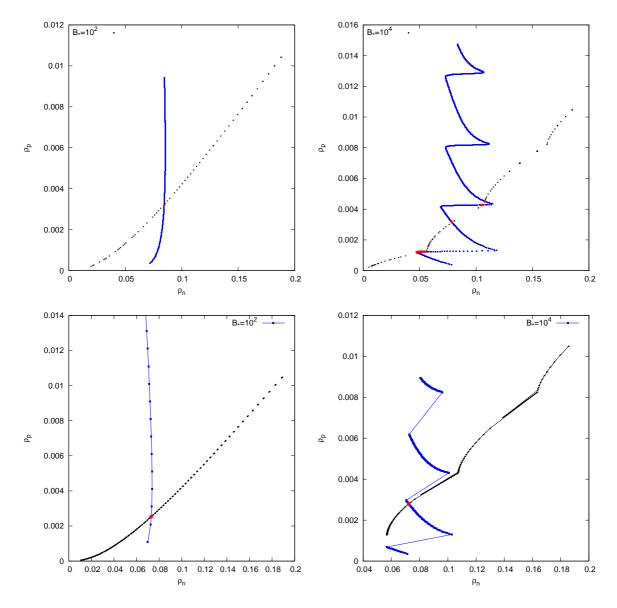


Figure 2: The crossing of the β -equilibrium line with the thermodynamic (upper panels) and dynamical (lower panels) spinodal for relative magnetic field strength $B_* = 10^2$ (left column) and 10^4 (right column). The SLy5 functional is used.

In Figure 2 the solid blue lines determine the spinodals, the β -equilibrium lines are shown by the black points, while the crossing points are demarcated by the red dots. We can see that the qualitative behavior of the two spinodals is very similar, but the transition occurs at lower density when finite size fluctuations are taken into account (lower panels), as expected. Because of the non-monotonous behavior of the spinodals in the presence of magnetic fields, it is clear that several crossing points are possible. This is however not a general rule, as we can see from the lower right part of Fig. 2: a single transition point is observed even at very high magnetic fields for the dynamical spinodal of SLy5. This is at variance with the findings of ref.[34, 35, 36] and shows that the possibility of having successive layers of stable and unstable matter is model dependent.

In Tables 3 and 4, we list the first and the last crossing points as obtained from the thermodynamic and the dynamic analysis, as a function of the magnetic field. This defines the density $\Delta \rho_{PT}$ and pressure Δp_{PT} interval corresponding to the successive sequence of stable and unstable thermodynamic

configurations, due to the presence of Landau levels.

Table 3: The uncertainty in the transition point for thermodynamical spinodals of the SLy5 functional, for different magnetic field strengths (see text for more details).

B^*	$ ho_1$	ρ_2	Δho_{PT}	p_1	p_2	Δp_{PT}
	(fm^{-3})	(fm^{-3})	(fm^{-3})	(MeV/fm^{-3})	(MeV/fm^{-3})	(MeV/fm^{-3})
10^{2}	0.088	0.088	0.	0.462	0.462	0.
10^{3}	0.086	0.091	0.005	0.442	0.502	0.06
5×10^3	0.075	0.112	0.037	0.332	0.882	0.550
7×10^{3}	0.070	0.090	0.020	0.300	0.501	0.201
10^{4}	0.048	0.113	0.065	0.193	0.937	0.744

As previously observed in ref.[34, 35, 36], the global effect of the magnetic field is to increase the density and pressure region where the EoS behavior is not monotonic, but the effect is non-linear. We observe that this effect is somewhat quenched in the dynamical spinodal treatment with respect with the thermodynamical one.

Table 4: Density and pressure of the transition point for dynamical spinodals of the SLy5 functional, for different magnetic field strengths (see text for more details).

B^*	$ ho_1$	ρ_2	Δho_{PT}	p_1	p_2	Δp_{PT}
	(fm^{-3})	(fm^{-3})	(fm^{-3})	(MeV/fm^{-3})	(MeV/fm^{-3})	(MeV/fm^{-3})
10^{2}	0.079	0.079	0.	0.356	0.356	0.
10^{3}	0.075	0.077	0.002	0.320	0.338	0.018
5×10^3	0.071	0.085	0.014	0.297	0.438	0.141
7×10^3	0.065	0.085	0.020	0.261	0.439	0.178
10^{4}	0.043	0.077	0.034	0.165	0.369	0.204

3.2 Sensitivity of CCPT to influential parameters

It was shown by different authors [26, 27, 51, 52] that the core-crust phase transition in ordinary non-magnetized neutron stars strongly depends on the symmetry energy, particularly on the slope parameter L_{sym} . Within the MM approach, in a recent analysis [29] a systematic study was performed in order to isolate the effects of the empirical nuclear parameters and their uncertainties. It was found that the most influential parameters are the poorly known isovector parameters L_{sym} and K_{sym} . In this section, we study the effect of L_{sym} and K_{sym} on the CCPT density as estimated from the thermodynamic spinodal, as a function of the magnetic field.

We take as fiducial values the ones of the SLy5 functional, $L_{sym}=48.3~{\rm MeV}$ and $K_{sym}=-112~{\rm MeV}$. To study the sensitivity to those parameters, we modify the parameters one by one keeping all the others unchanged. For the parameter under study, we consider two extreme values corresponding to the present uncertainty from nuclear physics experiments as estimated in ref. [37], namely $L_{sym}^{min}=47~{\rm MeV},~L_{sym}^{max}=106~{\rm MeV},~K_{sym}^{min}=-135~{\rm MeV},~K_{sym}^{max}=129~{\rm MeV}.$

We can see from the results of Figures 3 and 4 that the transition point is strongly modified by a change of the slope parameter L_{sym} . As a general statement, a stiffer symmetry energy leads to higher values for the transition density, as already observed in the literature [26, 27, 51, 52]. We can additionally observe that the effect strongly increases for the highest magnetic fields. For small values of L_{sym} such as SLy5 or L_{sym}^{min} , the transition densities ρ_1 and ρ_2 coincide, but for large values of L_{sym} they are quite different for different magnetic field strengths B_* . In particular, we can see that the existence of successive stable and instable regions around the transition point seems to be strongly

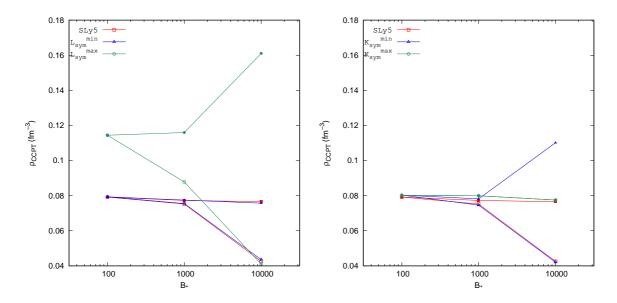


Figure 3: Sensitivity of the CCPT density from the dynamical spinodal analysis to L_{sym} (left) and K_{sym} (right). Open (filled) symbols represent the first (last) crossing of the beta-equilibrium line with the spinodal envelope.

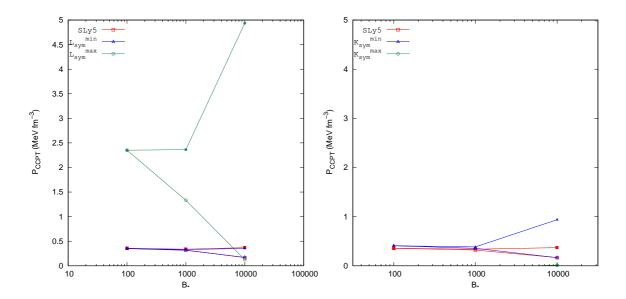


Figure 4: Sensitivity of the CCPT pressure from the dynamical spinodal analysis to L_{sym} (left) and K_{sym} (right). Open (filled) symbols represent the first (last) crossing of the beta-equilibrium line with the spinodal envelope.

correlated with the L_{sym} parameter. Concerning K_{sym} , we can see that it is by far less influential than L_{sym} . Variations of K_{sym} in the physically reasonable range K_{sym}^{min} to K_{sym}^{max} does not change the CCPT density considerably for different magnetic field strengths B_* . An important effect is only seen for the highest magnetic field, when two different transition points start to appear due to the highly complex behavior of the spinodal zone.

From Figure 3 we can conclude that better constraints on the symmetry energy slope L_{sym} are expected to strongly reduce the model dependence of the results.

4 Magnetic field effects on the mass-radius relation

In the previous section, we demonstrated how much a strong magnetic field affects the thermodynamical and dynamical spinodals and hence the crust-core phase transition in neutron stars. We can therefore expect following the previous studies [34, 35, 36] that the magnetic field will also play an important role in determining the structure of neutron stars, especially its radius and crust thickness. In order to investigate the influence of magnetic field on the static properties of strongly magnetized neutron stars, we choose as a reference model for this section the Skyrme SLy4 EoS, which is one of the most commonly used EoS in astrophysics [53].

Structure calculations of strongly magnetized neutron stars have been discussed intensively in the literature in the past few years [54, 55, 56, 57, 58, 40, 41]. It is well known that strong electromagnetic field affects neutron stars in two ways: firstly the EoS due to the quantization of the charged particles into Landau levels, and secondly by introducing an anisotropy in the energy momentum tensor and thereby affecting the global structure. In the presence of strong magnetic fields, the neutron star shape strongly deviates from spherical symmetry and hence the spherically symmetric Tolman-Oppenheimer-Volkov (TOV) equations are no longer applicable. The ideal method to tackle the problem is to self-consistently solve the neutron star structure equations endowed with a magnetic field, i.e. Einstein-Maxwell and equilibrium equations, with a magnetic field dependent EoS. However this is a complicated numerical problem that has only been tackled recently [40, 41]. In this section, we compute and compare the mass-radius relations of magnetized neutron stars obtained using both an isotropic TOV solution [34, 35, 36], as well as a full numerical solution.

4.1 TOV calculation

In the calculation of the core EoS, the magnetic field contribution to the energy density and pressure, $\epsilon_B = p_B = B^2/8\pi$, is assumed to be isotropic:

$$\epsilon_{tot} = ne_{HNM} + \epsilon_l + \epsilon_B;
p_{tot} = p_{HNM} + p_l + p_B.$$
(14)

Here, e_{HNM} (p_{HNM}) is the hadronic contribution to the energy (pressure) from the MM EoS eq.(1), modified such as to include the magnetic field contribution as in eq.(9). The lepton contribution ϵ_l , p_l is calculated considering electrons as a relativistic free Fermi gas, again modified by the magnetic field as explained in section 2.3.

Using the core EoS and the CCPT points calculated in the previous subsection for the SLy4 case, we aim to compute the mass-radius relations of magnetized neutron stars. The calculation of the structure of neutron stars using TOV requires the additional knowledge of the crust EoS. This can however be avoided by using the method proposed by Zdunik et al. [25]. In this method, one integrates from the core to the crust-core interface following the TOV prescription in order to obtain the core mass and radius. A simple algebraic calculation relates the crust mass M_{crust} and the total radius

 R_{NS} with the core mass M_{core} and core radius R_{core} and the CCPT density ρ_{cc} and pressure P_{cc} as:

$$\begin{split} M_{crust} &= \frac{4\pi P_{cc} R_{core}^4}{G M_{core}} \left(1 - \frac{2G M_{core}}{R_{core} c^2}\right) \\ R_{NS} &= \frac{R_{core}}{1 - (\alpha - 1)(R_{core} \, c^2 \, G \, M_{NS} - 1)} \end{split}$$

where $\alpha = \left(\frac{\mu_{cc}}{\mu_0}\right)^2$ is the ratio of the baryon chemical potentials at the crust-core interface and that of cold catalyzed matter at zero pressure (930.4 MeV). The crust thickness is then easily obtained from the relation $l_{crust} = R_{NS} - R_{core}$.

This approximation was shown to be reasonably precise for not too low neutron star masses in ref. [25].

In Fig. 5 the mass-radius relation of neutron stars endowed with different magnetic field strengths computed within the spherical TOV approximation using the Zdunik method for the SLy4 EoS are shown. Notice that the maximum mass is not always reached, a limitation of the meta-modelling due to the fact that the convergence of the Taylor expansion is not perfect at the highest densities. However, this is not a problem here, since we are mainly interested in the radius, which depends mainly on the low density region. For comparison the mass-radius relation using the Douchin Haensel (DH) SLy4 EoS [53] for B=0 is also plotted. This EoS is based on the same SLy4 energy functional, but the inhomogeneous crust contribution is explicitly accounted for. The close agreement between the DH result and our result at the lowest magnetic field demonstrated the quality of the Zdunik approximation. We can also see from the figure that except the case of very strong magnetic fields $B_* \sim 10^4$, the effect of magnetic field on the total mass and radius of the neutron star is almost negligible in the spherical TOV approximation, in agreement with the results of ref. [34, 35, 36]. However, the magnetic field has a non-negligible effect on the dynamical spinodals and hence the crust-core phase transition, which in turn should affect the crust-thickness. In Table 5, we summarize the effect of different magnetic field strengths on the transition densities and the neutron star structure. For zero or low magnetic fields $(B_* \sim 10^2, 10^3)$, there is a unique transition density. However for higher fields, as discussed in Sec. 3.1, the β -equilibrium line crosses the dynamical spinodals at multiple points. The transition density corresponding to the first and the last crossings are denoted as ρ_1 and ρ_2 in the table. The difference in crust-core transition density leads to a difference in the corresponding total and core radii and crust thickness $l_{crust} = R_{NS} - R_{core}$. The values of l_{crust}^1 and l_{crust}^2 , corresponding to ρ_1 and ρ_2 , are also given in the table, along with their difference $\Delta l_{crust} = l_{crust}^2 - l_{crust}^1$. In this case, both l_{crust}^1 and l_{crust}^2 are of the order of 1 Km, much thinner than what was suggested in [33]. Δl_{crust} measures the region in the neutron star crust where layers of homogeneous and inhomogeneous matter might coexist [34, 35, 36]. These results are in good qualitative agreement with ref. [34, 35, 36], even if some quantitative differences arise from the use of a different functional. The model dependence of the results will be discussed in section 4.3.

Table 5: Effect of a strong magnetic field on the transition density and crust thickness for a neutron star of gravitational mass 1.4 M_{\odot} with the SLy4 functional, in the isotropic TOV approximation. See text for details.

B_*	$\begin{array}{c} \rho_1 \\ (\text{fm}^{-3}) \end{array}$	R_{NS}^{1} (km)	R_{core}^{1} (km)	l_{crust}^{1} (km)	$\begin{array}{c} \rho_2 \\ (\text{fm}^{-3}) \end{array}$	R_{NS}^2 (km)	R_{core}^2 (km)	l_{crust}^2 (km)	Δl_{crust} (km)
0	0.077	11.704	10.797	0.908	0.077	11.704	10.797	0.908	0
10^{2}	0.076	11.771	10.843	0.928	0.076	11.771	10.843	0.928	0
10^{3}	0.071	11.770	10.859	0.911	0.074	11.770	10.849	0.920	0.009
5×10^3	0.070	11.764	10.865	0.899	0.084	11.761	10.8	0.961	0.062
7×10^3	0.033	11.804	10.993	0.811	0.081	11.777	10.811	0.966	0.155
10^{4}	0.041	11.826	10.97	0.856	0.074	11.795	10.855	0.940	0.084

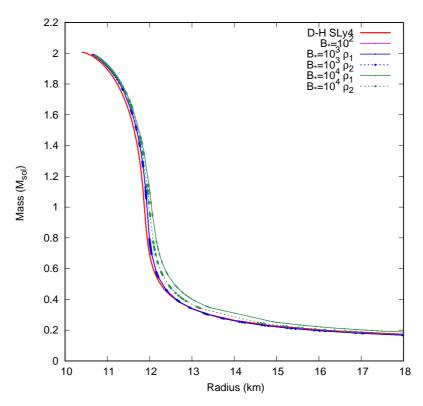


Figure 5: Mass-radius relation of neutron stars endowed with various magnetic field strengths computed using the isotropic TOV approximation and the Zdunik method for the SLy4 EoS. For comparison the mass-radius relation using the Douchin Haensel SLy4 EoS for B=0 from ref.[53] is also plotted.

One may also calculate the fractional moment of inertia of the crust I_{crust}/I using the formula [6]

$$I_{crust} = \frac{16\pi}{3} \frac{R_{core}^6 p_{PT}}{R_s} \left[1 - \frac{0.21}{(R/R_s - 1)} \right] \left[1 + \frac{48}{5} (R_{core}/R_s - 1)(p_{PT}/\epsilon_{PT} + \dots) \right] , \qquad (15)$$

where, the total moment of inertia of the star is

$$\frac{I}{MR^2} = \frac{0.21}{1 - R_s/R} \ . \tag{16}$$

In the above expressions, $R_s = 2GM$ is the Schwarzschild radius of the star.

Table 6: Effect of strong magnetic field on transition density and fractional moment of inertia of the crust for a neutron star of gravitational mass 1.4 M_{\odot} with the SLy4 functional, in the isotropic TOV approximation. See text for details.

B_*	$\begin{array}{c} \rho_1 \\ (\text{fm}^{-3}) \end{array}$	I^1_{crust}/I	$\begin{array}{c} \rho_2 \\ (\mathrm{fm}^{-3}) \end{array}$	I_{crust}^2/I	$\Delta I_{crust}/I$
0	0.077	0.028	0.077	0.028	0
10^{2}	0.076	0.028	0.076	0.028	0
10^{3}	0.071	0.026	0.074	0.027	0.001
5×10^3	0.070	0.025	0.084	0.036	0.011
7×10^3	0.033	0.011	0.081	0.035	0.024
10^{4}	0.041	0.015	0.074	0.030	0.015

4.2 Full numerical calculations

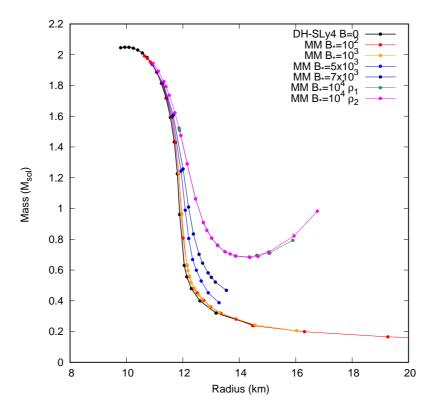


Figure 6: Circumferential radius vs gravitational mass of neutron stars endowed with strong magnetic fields computed using the complete MM (crust and core), and the full solution of the Einstein-Maxwell equations with LORENE, for the SLy4 EoS. For comparison the Douchin Haensel SLy4 for B=0 is also plotted.

As was already discussed, the isotropic TOV equations are not valid for strongly magnetized neutron stars for which the energy-momentum tensor is anisotropic. There have been several suggestions in the literature to remedy the situation. Common procedures are to consider that the magnetic field contribution to the energy density and pressure is anisotropic in the parallel and perpendicular directions to the magnetic field:

$$\epsilon_{tot} = \epsilon_{had} + \epsilon_l + \epsilon_B
p_{\parallel} = p_{had} + p_l - p_B
p_{\perp} = p_{had} + p_l - \mathcal{M}B + p_B$$
(17)

either neglecting or considering the contribution to the EoS from magnetization (the term $\mathcal{M}B$) [55].

Another alternative is the chaotic magnetic field formalism [55]:

$$\epsilon_{tot} = \epsilon_{had} + \epsilon_l + \epsilon_B
p_{tot} = p_{had} + p_l + p_B/3$$
(18)

However, the ideal way to calculate the structure of strongly magnetized neutron stars is to solve the Einstein-Maxwell and equilibrium solutions self-consistently with a magnetic field dependent EoS. We adopt this technique as we have at our disposal the numerical library LORENE [59] previously developed for studying the structure of strongly magnetized neutron stars [60, 61, 40, 41]. To this aim, we first construct total EoSs for neutron stars for the crust and the core obtained using the same MM. This is done using the compressible liquid drop model for the crust, with surface tension parameters

optimized for each functional via a fit on nuclear masses [28]. The magnetic field dependence is only included in the core EoSs while assuming a non-magnetized crust, which is a reasonable approximation.

We display the mass-radius relations corresponding to the SLy4 EoSs for increasing magnetic fields in Fig. 6. It is evident from the figure that while neutron star mass-radius relation for low fields $B_* = 10^2, 10^3$ resembles that of the zero-field case, for higher magnetic fields $B_* = 5 \times 10^3, 7 \times 10^3, 10^4$ the mass-radius relation departs strongly from the zero field case. As was discussed in [40, 41], this is primarily due to the purely magnetic field contribution and not the effect of magnetic field on the EoS.

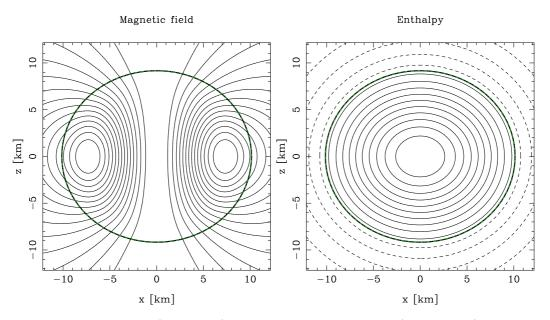


Figure 7: Magnetic field lines (left panel) and enthalpy isocontours (right panel) in the meridional plane (x, z), for the static star configuration, with a gravitational mass of 1.4 M_{\odot} and a polar magnetic field $B_* = 10^4$. The stellar surface is depicted by the bold line. In the right panel, solid lines represent positive enthalpy isocontours, dashed lines negative ones.

One must also note that while for the isotropic TOV calculation one assumed a constant magnetic field, the magnetic field for the full numerical calculation is generated via a current function and hence generates a profile, from the highest central value decreasing towards the surface [42]. In Fig. 7 we display the magnetic field lines and enthalpy isocontours of a neutron star of gravitational mass of 1.4 M_{\odot} and a polar magnetic field $B_* = 10^4$ (i.e. 4.414×10^{13} T). It is evident that the magnetic field is far from constant, and the neutron star surface deviates from a spherical shape, as elaborated previously. As the neutron star radius as well as the magnetic field are direction dependent, we specify for this study the radius as the circumferential equatorial radius R_{circ} (see [61]). In Fig. 8, we display the radial profiles of the first four even multipoles (l = 0, 2, 4, 6) of the magnetic field norm $b(r, \theta)$ computed for the stellar model described in Fig.7. From symmetry argument odd multipoles are all zero [42]. We also plot the magnetic field norm as a function of the coordinate radius for different angular directions ($\theta = 0, \pi/4, \pi/2$). It is clear that the magnetic field structure in this case can neither be described by a constant amplitude nor a simple profile.

Similar to Table 5, we summarize in Table 7 the effect of different magnetic field strengths on the transition densities and the neutron star structure computed within the full numerical structure calculation via LORENE. As before, for low magnetic fields ($B_* \sim 10^2, 10^3$), there is a unique transition density. At higher fields, as discussed in Sec. 3.1, there are multiple transition density points, of which the first and the last crossings are denoted as ρ_1 and ρ_2 in the table. The difference in crust-core transition density leads to a difference in the corresponding total circumferential radii R_{NS} ,

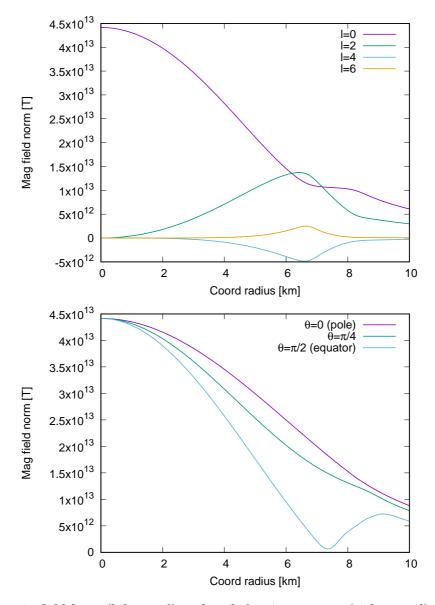


Figure 8: Magnetic field lines (left panel) and enthalpy isocontours (right panel) in the meridional plane (x, z), for the static star configuration, with a gravitational mass of 1.4 M_{\odot} and a polar magnetic field $B_* = 10^4$.

circumferential core radii R_{core} and crust thickness l_{crust} . The values of l_{crust}^1 and l_{crust}^2 , corresponding to ρ_1 and ρ_2 , are also given in the table, along with their difference $\Delta l_{crust} = l_{crust}^2 - l_{crust}^1$.

As compared to the previous Table 5, one can see here that although the total radii are comparable, the core radii and hence the crust thickness calculated numerically differ significantly from the isotropic TOV case. This is due to the difference in the treatment of the magnetic field profile as well as the pure magnetic field contribution. In particular, the difference in the crust thickness Δl_{crust} is significantly higher. Actually, both l_{crust}^1 and l_{crust}^2 are now of the order of 3 Km, considerably thicker than what was obtained with the TOV treatment for an isotopic star and also larger than the 2.4 Km, estimated in [33].

Table 7: Effect of strong magnetic field on total circumferential radius, circumferential core radius and crust thickness for a neutron star of gravitational mass 1.4 M_{\odot} computed within a full numerical

structure calculation with LORENE.

B_*	$\begin{array}{c} \rho_1 \\ (\text{fm}^{-3}) \end{array}$	R_{NS}^1 (km)	R_{core}^1 (km)	l_{crust}^1 (km)	$\begin{array}{c} \rho_2 \\ (\text{fm}^{-3}) \end{array}$	R_{NS}^2 (km)	R_{core}^2 (km)	l_{crust}^2 (km)	Δl_{crust} (km)
10^{2}	0.076	11.791	8.577	3.214	0.076	11.791	8.577	3.214	0
10^{3}	0.074	11.782	8.595	3.187	0.074	11.782	8.595	3.187	0
5×10^3	0.070	11.836	8.705	3.131	0.084	11.841	8.448	3.393	0.262
7×10^{3}	0.033	11.900	8.585	3.315	0.081	11.896	8.320	3.576	0.261
10^{4}	0.041	12.039	8.300	3.739	0.074	12.037	8.129	3.908	0.169

4.3 Model dependence of the results

In order to generalize the results obtained for any EoS, we perform the isotropic approximation and full numerical calculation for two other reference parameter sets, TM1 and Bsk17 (see Sec.2.1). The corresponding mass-radius relations for various magnetic field values obtained numerically are given in the figures 9 and 10 and the main results are summarized in Tables 8 and 9.

Table 8: Effect of strong magnetic field on total circumferential radius, circumferential core radius and crust thickness for a neutron star of gravitational mass 1.1 M_{\odot} computed numerically, for the Bsk17 EoS.

B_*	$ \begin{array}{c} \rho_1\\ (\text{fm}^{-3}) \end{array} $	R_{NS}^{1} (km)	R_{core}^1 (km)	l_{crust}^1 (km)	$ \begin{array}{c} \rho_2\\ (\text{fm}^{-3}) \end{array} $	R_{NS}^2 (km)	R_{core}^2 (km)	l_{crust}^2 (km)	Δl_{crust} (km)
10^{2}	0.090	10.995	8.660	2.335	0.090	10.995	8.660	2.335	0
10^{3}	0.085	10.990	8.677	2.313	0.087	10.990	8.677	2.313	0
5×10^3	0.078	11.060	8.533	2.527	0.093	11.059	8.510	2.549	0.022
7×10^3	0.071	11.136	8.413	2.723	0.091	11.143	8.396	2.747	0.024
10^{4}	0.048	11.244	8.179	3.065	0.115	11.276	8.090	3.186	0.121

As it is already very well known, the stiffest model (TM1) produces the largest radius for a given mass. We can see from Figs.9 and 10 that this model dependence is preserved with the increase of the magnetic field. The width of the crust monotonically increases with the magnetic field for all studied models, and it seems to be very well correlated with the star radius, a stiffer EoS producing a thicker crust. Conversely, the region where successive homogeneous and inhomogeneous layers are expected [34, 35, 36], measured by the variable Δl_{crust} , seems to decrease with increasing stiffness.

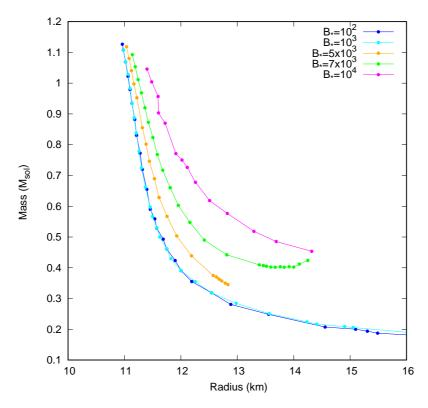


Figure 9: Circumferential radius vs gravitational mass of neutron stars endowed with strong magnetic fields computed using the MM for Bsk17 EoS.

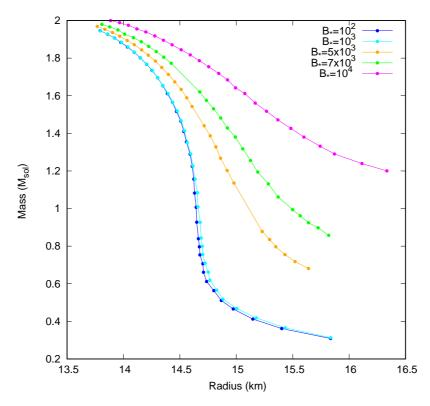


Figure 10: Circumferential radius vs gravitational mass of neutron stars endowed with strong magnetic fields computed using the MM for TM1 EoS.

Table 9: Effect of strong magnetic field on total circumferential radius, circumferential core radius and crust thickness for a neutron star of gravitational mass 1.8 M_{\odot} computed numerically, for the TM1

EoS.

B_*	$\begin{array}{c} \rho_1 \\ (\text{fm}^{-3}) \end{array}$	R_{NS}^{1} (km)	R_{core}^{1} (km)	l_{crust}^{1} (km)	$\begin{array}{ c c c c c c c c c c c c c c c c c c c$	R_{NS}^2 (km)	R_{core}^2 (km)	l_{crust}^2 (km)	$\begin{pmatrix} \Delta l_{crust} \\ (\mathrm{km}) \end{pmatrix}$
10^{2}	0.066	14.153	10.777	3.376	0.066	14.153	10.777	3.376	0
10^{3}	0.057	14.157	10.781	3.376	0.063	14.157	10.781	3.376	0
5×10^3	0.055	14.252	10.625	3.627	0.093	14.251	10.595	3.656	0.029
7×10^{3}	0.061	14.357	10.444	3.913	0.099	14.357	10.415	3.942	0.029
10^{4}	0.038	14.594	10.119	4.475	0.102	14.856	10.055	4.531	0.056

For the numerical calculations of the strongly magnetized neutron stars using LORENE, one may calculate the total moment of inertia of a slowly rotating neutron star from the total angular momentum, taking into account both contributions from rotation and magnetic field. However, within the numerical models (see [40] and references within), one cannot isolate the crustal moment of inertia in a gauge-independent way. Hence we refrain from performing a calculation of the fractional crustal moment of inertia as was done in Sec. 4.1 for the TOV calculations.

5 Final remarks

In this work, we extended a recently developed meta-modelling technique to study the crust-core phase transition properties and crustal thickness in the presence of strong magnetic fields. It was found that the magnetic field severely modifies the structure of the phase transition region, leading to the a non-negligible difference in the density and pressure of the transition from that of the zero magnetic field case. As previously observed in refs.[34, 35, 36], the most spectacular effect of the magnetic field is the fact that the instable region with respect to density fluctuations is discontinuous if the magnetic field is sufficiently intense. As a consequence, beta equilibrated matter can correspond to a sequence of stable and unstable regions, as a function of the density. How this feature will reflect in the composition of the neutron star is not clear. It might be that the crust is simply more extended, or that in its inner part homogeneous and inhomogeneous layers could coexist, with much higher impurity factors than usually considered for non-magnetized star.

A sensitivity analysis to the most influential isovector empirical parameters (L_{sym} and K_{sym}) has shown that the discontinuity in the instable region is strongly increasing with the L_{sym} parameter, and the effect is amplified by the intensity of the magnetic field.

In order to study the effect of the change in crust-core transition properties on the neutron star structure, we adopted two different formalisms. Firstly we calculated the mass-radius relation as well as the crust thickness using an isotropic TOV formalism, that has been commonly used in the literature. Next we performed a full self-consistent numerical computation of the neutron star structure. We showed that the results in the two cases vary considerably, and underlined the fact that a full numerical formalism is inevitable for the structure calculation of strongly magnetized neutron stars.

Acknowledgments

This work was partially supported by the NewCompStar COST action MP1304, Capes(Brazil)/Cofecub (France), joint international collaboration project number 853/15 and project INCT-FNA Proc. No. 464898/2014-5. DC acknowledges the financial support from the CNRS/In2p3 through the Master project MAC and DPM was partially supported by CNPq (Brazil) under grant 301155/2017-8. DPM thanks the LPC-Caen for the hospitality.

The authors thank Sofija Antić for providing useful data for comparison with the non-magnetic field case and Thomas Carreau for providing the crust EoS for the different functionals used in this work.

References

- [1] K. C. Gendereau, Z. Arzoumanian and T. Okajima, Proc. SPIE 8443 (2012) 844313
- [2] F. Ozel et al., Astrophys. J. 832 (2016) 92
- [3] D. Bandyopadhyay, S. A, Bhat, P. Char and D. Chatterjee, Eur. Phys. J. A. 54 (2018) 26
- [4] M. Fortin et al., Phys. Rev. C 94 (2016) 035804
- [5] F. Gulminelli et al., J. Phys.: Conf Ser. 420 (2013) 012079
- [6] F. J. Fattoyev and J. Piekarewicz, Phys.Rev.C 82 (2010) 025810
- [7] A. Potekhin, J. Pons and D. Page, Space Sci. Rev. 91 (2015) 239
- [8] R. Bondarescu and I. Wasserman, Astrophys. J. 778 (2013) 9.
- [9] B. P. Abbott et al. (LIGO Scientific Collaboration and Virgo Collaboration), Phys. Rev. Lett. 119, 161101 (2017).
- [10] P. S. Cowperthwaite et al. (Ligo Scientific Collaboration and Virgo Collaboration), Astrophys. Jour. Lett. 848: L12 (2017).
- [11] T. Damour, M. Soffel and C.-M. Xu, Phys. Rev. D 45, 1017 (1992).
- [12] E.E. Flanagan and T. Hinderer, Phys. Rev. D 77, 021502 (2008).
- [13] Mariana Dutra, Cesar V. Flores, César Lenzi, Odilon Lourenço and Débora P. Menezes, in preparation.
- [14] G. Baym, C. Pethick and P. Sutherland, Astrophys. J. 170, 299 (1971).
- [15] G. Baym, H.A. Bethe and C. Pethick, Nucl. Phys. A 175, 225 (1971).
- [16] C. Ducoin, J. Margueron and C. Providência, Eur. Phys. Lett. 91 (2010) 32001
- [17] Constanca Providência and Debora P. Menezes, Phys. Rev. C 96, 045803 (2017); S.S. Avancini, S. Chiacchiera, D.P. Menezes and C. Providência Phys. Rev. C 82, 055807 (2010); Erratum: Phys. Rev. C 85, 059904(E) (2012).
- [18] S.S. Avancini, D.P. Menezes, M.D. Alloy, J.R. Marinelli, M.M.W. de Moraes and C. Providência, Phys. Rev. C 78, 015802 (2008).
- [19] D.G. Ravenhall, C.J. Pethick and J.M. Lattimer, Nucl. Phys. A 407 (1983) 571.
- [20] C. P. Lorenz, D. G. Ravenhall, and C. J. Pethick, Phys. Rev. Lett. 70, 379 (1993).
- [21] D. G. Ravenhall and C. J. Pethick, Astrophys. J. 424, 846 (1994).
- [22] B. Link, R. I. Epstein, and J. M. Lattimer, Phys. Rev. Lett. 83, 3362 (1999).
- [23] J. M. Lattimer and M. Prakash, Phys. Rep. 442, 109 (2007).
- [24] F. J. Fattoyev and J. Piekarewicz, Phys. Rev. C 82, 025810 (2010).
- [25] L. Zdunik, M. Fortin and P. Haensel, A&A 599 (2017) A119

- [26] C. Ducoin, J. Margueron and Ph. Chomaz, Nucl. Phys. A 809 (2008) 30.
- [27] C. Ducoin et al., Phys. Rev. C 83 (2011) 045810.
- [28] T. Carreau, F. Gulminelli, J. Margueron, arXiv:1810.00719.
- [29] S. Antic, D. Chatterjee, T. Carreau and F. Gulminelli, in preparation
- [30] SGR/APX on-line catalogue, http://www.physics.mcgill.ca/~pulsar/magnetar/main.html .
- [31] S. Chakrabarty, D. Bandyopadhyay and S. Pal, Phys. Rev. Lett. 78 (1997) 2898.
- [32] J.A. Pons, D. Viganò and N. Rea, Nature Phys. 9, 431 (2013).
- [33] J. Piekarewicz, F. J. Fattoyev and C.J. Horowitz, Phys. Rev. C 90, 015803 (2014).
- [34] Jianjun Fang, Helena Pais, Sidney Avancini and Constança Providência, Phys. Rev. C 94, 062801 (R) (2016).
- [35] Jianjun Fang, Helena Pais, Sagar Pratapsi, Sidney Avancini, Jing Li and Constança Providência, Phys. Rev. C 95, 045802 (2017).
- [36] Jianjun Fang, Helena Pais, Sagar Pratapsi and Constança Providência, Phys. Rev. C 95, 045802 (2017).
- [37] J. Margueron, R. Hoffmann Casali and F. Gulminelli, Phys. Rev. C 97, 025805 (2018).
- [38] J. Margueron, R. Hoffmann Casali and F. Gulminelli, Phys. Rev. C 97, 025806 (2018).
- [39] D. Chatterjee, F. Gulminelli, Ad. R. Raduta, J. Margueron, Phys. Rev. C 96, 065805 (2017).
- [40] D. Chatterjee, T. Elghozi, J. Novak and M. Oertel, MNRAs 447 (2015) 3785
- [41] D. Chatterjee, A. Fantina, N. Chamel, J. Novak and M. Oertel, MNRAS 469 (2017) 95
- [42] D. Chatterjee, J. Novak and M. Oertel, arXiv:1808.01778
- [43] E. Chabanat, P. Bonche, P. Haensel, J. Meyer, and R. Schaeffer, Nucl. Phys. A 635, 231 (1997).
- [44] S. Goriely, N. Chamel, and J. M. Pearson, Phys. Rev. Lett. 102 (2009) 152503.
- [45] Y. Sugahara and H. Toki, Nucl. Phys. A 579 (1994) 557
- [46] C. Drischler, K. Hebeler and A. Schwenk, Phys. Rev; C 93, (2016) 054314
- [47] C. Ducoin, P. Chomaz and F. Gulminelli, Nucl. Phys. A 789 (2007) 403
- [48] C.J.Pethick, D.G.Ravenhall, C.P.Lorentz, Nucl. Phys. A584 (1995) 675-703.
- [49] S. Chakrabarty, D. Bandhyopadhyay, S. Pal, Phys. Rev. Lett. 78 (1997) 2898; A. Broderick, M. Prakash, J.M. Lattimer, Astroph. J. 537 (2000) 351.
- [50] M.A. Perez Garcia, Phys. Rev. C 77 (2008) 065806; A.A. Isayev, J. Yang, Phys. Lett. B 707 (2012) 163.
- [51] J. Xu, L.-W. Chen, B.-A. Li, and H.-R. Ma, Astrophys. J. 697, 1549 (2009).
- [52] J. M. Pearson, N. Chamel, S. Goriely, and C. Ducoin, Phys. Rev. C 85, 065803 (2012).
- [53] F. Douchin and P. Haensel, A&A 380 (2001) 151.
- [54] L. Lopes and D. Menezes, Journal of Cosmology and Astroparticle Physics, 2015 08-002

- [55] D. P. Menezes and L. L. Lopes, Eur. Phys. J. A 52 (2016) 17
- [56] V. Dexheimer, R. Negreiros and S. Schramm, Eur. Phys. J. A 48 (2012) 189
- [57] D. P. Menezes and M. D. Alloy, arXiv:1607.07687
- [58] V. Dexheimer et al., Proceedings of the 4th Caribbean Symposium on Cosmology, Gravitation, Nuclear and Astroparticle Physics (STARS2017) and 5th International Symposium on Strong Electromagnetic Fields and Neutron Stars (SMFNS2017)
- [59] LORENE: http://www.lorene.obspm.fr
- [60] M. Bocquet, S. Bonazzola, E. Gourgoulhon, J. Novak, A&A 301 (1995) 757
- [61] S. Bonazzola S., E. Gourgoulhon, M. Salgado, J. A. Marck, A&A 278 (1993) 421